JOURNAL OF GEOPHYSICAL RESEARCH: SPACE PHYSICS, VOL. 118, 7654–7664, doi:10.1002/2013JA019372, 2013

# STEREO and Wind observations of intense cyclotron harmonic waves at the Earth's bow shock and inside the magnetosheath

A. W. Breneman,[1] C. A. Cattell,[1] K. Kersten,[1] A. Paradise,[1] S. Schreiner,[1] P. J. Kellogg,[1] K. Goetz,[1] and L. B. Wilson III[2]

Received 27 August 2013; revised 12 November 2013; accepted 24 November 2013; published 12 December 2013.

[1] We present the first observations of electron cyclotron harmonic waves at the Earth's bow shock from STEREO and Wind burst waveform captures. These waves are observed at magnetic field gradients at a variety of shock geometries ranging from quasi-parallel to nearly perpendicular along with whistler mode waves, ion acoustic waves, and electrostatic solitary waves. Large amplitude cyclotron harmonic waveforms are also observed in the magnetosheath in association with magnetic field gradients convected past the bow shock. Amplitudes of the cyclotron harmonic waves range from a few tens to more than 500 mV/m peak-peak. A comparison between the short (15 m) and long (100 m) Wind spin plane antennas shows a similar response at low harmonics and a stronger response on the short antenna at higher harmonics. This indicates that wavelengths are not significantly larger than 100 m, consistent with the electron cyclotron radius. Waveforms are broadband and polarizations are distinctively comma-shaped with significant power both perpendicular and parallel to the magnetic field. Harmonics tend to be more prominent in the perpendicular directions. These observations indicate that the waves consist of a combination of perpendicular Bernstein waves and field-aligned waves without harmonics. A likely source is the electron cyclotron drift instability which is a coupling between Bernstein and ion acoustic waves. These waves are the most common type of high-frequency wave seen by STEREO during bow shock crossings and magnetosheath traversals and our observations suggest that they are an important component of the high-frequency turbulent spectrum in these regions.

**Citation:** Breneman, A. W., C. A. Cattell, K. Kersten, A. Paradise, S. Schreiner, P. J. Kellogg, K. Goetz, and L. B. Wilson III (2013), STEREO and Wind observations of intense cyclotron harmonic waves at the Earth's bow shock and inside the magnetosheath, *J. Geophys. Res. Space Physics*, *118*, 7654–7664, doi:10.1002/2013JA019372.

## 1. Introduction

[2] High-frequency plasma waves have been known for some time to play an important role in the dissipation of bulk flow energy across the bow shock [e.g., *Papadopoulos*, 1985]. Initial studies of turbulence at the bow shock [e.g., *Fredricks et al.*, 1970] used time-averaged spectral data and showed the presence of two strongly enhanced spectral components: electromagnetic waves at <200 Hz and electrostatic waves from 200 to 800 Hz. Part of the electromagnetic spectrum was identified with fluxgate magnetometer data on IMP 6 to be composed of whistler mode waves by *Fairfield* [1974]. The electrostatic component was identified by *Rodriguez and Gurnett* [1975] as ion acoustic waves because of a dominant polarization along the magnetic field. This identification was supported by *Fuselier and Gurnett* [1984] who determined that the ion acoustic waves had wavelengths on the order of $\lambda > 2\pi\lambda_D$, where $\lambda_D$ is the Debye length, using wave/antenna interference effects that occur when the wavelength is of the same order or shorter than the antenna length.

[3] Waveform measurements have the advantage over low cadence spectral data of not averaging over a certain time period. This is particularly important when sampling regions with strong gradients and hence short-scale lengths, like the bow shock. The first results using electric field waveforms (ISEE 1) at the bow shock were published by *Formisano and Torbert* [1982] who identified ion acoustic waves downstream of the transition region. Later *Wygant et al.* [1987] identified large amplitude electric field spikes from 32 Sample/s survey electric field data in the transition region, interpreted as Doppler-shifted lower hybrid or ion acoustic waves. Initial waveform results from the Wind satellite mission showed the existence of large amplitude electrostatic solitary waves at the shock transition region [*Bale et al.*, 1998]. These structures, which tend to appear as small amplitude broadband bursts in time-averaged spectral

[1]School of Physics and Astronomy, University of Minnesota, Minneapolis, Minnesota, USA.
[2]NASA Goddard Space Flight Center, Greenbelt, Maryland, USA.

Corresponding author: A. W. Breneman, School of Physics and Astronomy, University of Minnesota, 116 Church St. SE, Minneapolis, MN 55455, USA. (awbrenem@gmail.com)


2169-9380/13/10.1002/2013JA019372

**Table 1.** Data on All Burst Waveform Captures (# Captures) Observed During STEREO Spacecraft (SC) Bow Shock Crossings[a]

| Date SC | Time | $V_{sw}$ | # Captures | Sample rate | Length | $\theta_{Bn}$ | $\|E_{max}\|$ | $\|E_{min}\|$ | $\|E_{mean}\|$ | $\|E_{median}\|$ | GSE Position |
|---|---|---|---|---|---|---|---|---|---|---|---|
| 06 Nov A | 00 : 51 | 380 | 17(13) | 125 | 32.7 | 90 | 273(273) | 6(37) | 50(88) | 38(62) | [15.1,1.8,5.8] |
| 06 Nov B | 00 : 18 | 380 | 22(19) | 125 | 32.7 | 79 | 357(357) | 31(163) | 194(268) | 195(265) | [13.9,1.9,5.6] |
| | 14 : 48 | 370 | 24(17) | 125 | 32.7 | 30 | 364(364) | 16(109) | 118(176) | 109(163) | [11.8,–7.2,–4.7] |
| 17 Nov A | 05 : 51 | 390 | 38(19) | 250 | 16.4 | 58 | 381(381) | 9(50) | 95(197) | 79(191) | [14.1,–0.9,6.5] |
| 18 Nov A | 00 : 40 | 340 | 14(4) | 250 | 16.4 | 85 | 157(137) | 2(67) | 41(95) | 26(95) | [14.4,–11.0,–6.6] |
| 17 Nov B | 02 : 44 | 395 | 5(0) | 250 | 16.4 | 47 | 121(N/A) | 6(N/A) | 32(N/A) | 27(N/A) | [15.2,–0.9,6.3] |
| | 20 : 13 | 340 | 38(22) | 250 | 16.4 | 20 | 225(225) | 4(57) | 58(116) | 49(108) | [12.2,–10.3,–5.7] |
| 29 Nov A | 11 : 16 | 460 | 10(0) | 125 | 131 | 46 | 263(N/A) | 4(N/A) | 52(N/A) | 36(N/A) | [14.6,–2.0,7.0] |
| 30 Nov A | 03 : 58 | 400 | 2(2) | 31 | 2100 | 27 | 518(518) | 414(414) | 466(466) | 466(466) | [8.1,–0.1,5.3] |
| | 04 : 03 | 400 | 3(3) | 31 | 2100 | 27 | 444(444) | 126(126) | 324(324) | 400(400) | [8.1,–0.1,5.3] |
| | 04 : 15 | 405 | 3(3) | 31 | 2100 | 27 | 581(581) | 371(371) | 447(447) | 424(424) | [8.1,–0.1,5.3] |
| 29 Nov B | 10 : 59 | 450 | 6(0) | 125 | 131 | 24 | 249(N/A) | 21(N/A) | 83(N/A) | 73(N/A) | [14.5,–1.5,6.4] |
| 30 Nov B | 03 : 55 | 460 | 2(1) | 31 | 2100 | 27 | 520(520) | 325(520) | 422(520) | 422(520) | [8.1,–0.1,5.3] |

[a] $|E_{max}|$ and $|E_{min}|$ represent the maximum and minimum wave amplitudes (mV/m peak-peak) out of the set of burst captures at each shock. The mean $|E_{mean}|$ and median $|E_{median}|$ values are calculated from all of the burst captures at each shock. The values in the parentheses are for the subset of waves with clear comma-shaped polarization only. Solar wind velocity ($V_{sw}$) are from the ACE spacecraft. Shock normal angles ($\theta_{Bn}$) are estimated from the geometric model described in the text. Also listed are the burst sample rate (kSamples/s), length of each individual burst (ms), and GSE position (in units of Earth radii) of the spacecraft during the time of the observations.

data, modify the shock potential structure and can provide significant energy dissipation at the shock transition region. Waveform data from Polar [*Hull et al.*, 2006] and Cluster [*Giagkiozis et al.*, 2011] have also been used to identify large amplitude (∼80 mV/m) ion acoustic waves at the bow shock transition region. An important observation from these and other waveform analyses [*Wilson et al.*, 2007, 2010] is that these waves can be large amplitude and bursty. The combined influence of significant numbers of large amplitude waves can potentially provide an important contribution to overall energy dissipation at the bow shock.

[4] We present a survey of STEREO and Wind burst captures showing that, in addition to whistler mode radiation, ion acoustic waves, and electrostatic solitary waves, a significant portion of the electric field spectrum at the bow shock transition region consists of electron cyclotron harmonic waves. These waves are also observed downstream of the bow shock in the magnetosheath in association with strong magnetic field gradients. These waves are much larger in amplitude than any previously reported in the magnetosheath.

## 2. Instrumentation and Data Set

[5] STEREO observations come from 13 inbound and outbound passes through the bow shock as well as a single magnetosheath traversal, all during the phasing orbits early in the mission. STEREO Waves [*Bougeret et al.*, 2008] measures electric field from three 6 m cylindrical antennas [*Bale et al.*, 2008]. These antennas were designed to provide accurate measurement of the electric field at frequencies > 20 kHz. The accuracy of the electric field measurements at the frequencies of waves presented in this paper (∼1 kHz) is not as well established but it is likely that the amplitudes we present are close to their actual values (see Appendix A for details of the process of converting the raw antenna signal into an electric field).

[6] The Time Domain Sampler (TDS) provides short bursts of AC-coupled electric field at up to 250,000 samples per second. No search-coil magnetic field data are available on STEREO. The primary advantage of the STEREO data set is in providing a large number of three-dimensional burst captures during the shock crossings. Shock crossings are identified with a combination of In-situ Measurements of Particles and Coronal mass ejection Transients (IMPACT) fluxgate magnetometer data [*Luhmann et al.*, 2008] and Block Adaptive-tree Solar-wind Roe-type Upwind Scheme (BATS-R-US) MHD simulations (with solar wind input) of the interaction between the solar wind and the Earth's magnetosphere. In general, particle data are not available to facilitate this identification because the STEREO spacecraft were still in the commissioning phase during this time and the instruments were not fully operational. Despite this, flux levels are high enough on a few of the crossings that data from the Solar Wind Electron Analyzer (SWEA) [*Sauvaud et al.*, 2008] were used to corroborate the identification of the bow shock crossing.

[7] Wind observations come from a single bow shock crossing, identified from fluxgate magnetometer [*Lepping et al.*, 1995] and plasma instrumentation [*Ogilvie et al.*, 1995]. Wind measures electric field from a short spin-axis 12 m tip-tip antenna pair ($E_z$) and spin plane antenna pairs with tip-tip lengths of 100 m ($E_x$) and 15 m ($E_y$). Note that on 3 August 2000 and 25 September 2002, the long spin plane antenna was sheared by dust impacts, reducing its physical length (this effect is accounted for, as discussed in detail toward the end of Appendix A). Wind fast mode Time Domain Sampler measures short AC-coupled bursts of the spin plane electric field [*Bougeret et al.*, 1995] at 125,000 Samples/s. The different response on the long and short Wind spin plane antennas as a function of harmonic number allows us to place limits on the wavelength of the cyclotron harmonic waves.

[8] We also show evidence in Appendix B that the harmonics observed are real and not introduced by a harmonic instrumental response due to large amplitude or short wavelength waves.

## 3. STEREO and Wind Survey and Event Analysis

[9] Table 1 records shock properties as well as burst capture statistics at 13 STEREO bow shock crossings. Because no particle measurements are available, a rough estimate of the shock normal angle at the location of each crossing was determined by inputting magnetometer data into the hyperbolic shock model of *Slavin and Holzer* [1981]. All of the

**Table 2.** Data on All Burst Waveform Captures (# Captures) Observed by the STEREO Spacecraft (SC) Inside of the Magnetosheath[a]

| Date SC | Start Time | End Time | # Captures | Sample Rate | Length | $\|E_{max}\|$ | $\|E_{min}\|$ | $\|E_{mean}\|$ | $\|E_{median}\|$ | GSE Position Start | GSE Position End |
|---|---|---|---|---|---|---|---|---|---|---|---|
| 17 Nov A | 21 : 54 | 23 : 35 | 21(21) | 250 | 16.4 | 110(110) | 45(45) | 67(67) | 65(65) | [11.3,–9.3,–6.1] | [13.6,–10.6,–6.5] |
| 17 Nov B | 04 : 07 | 04 : 38 | 21(6) | 250 | 16.4 | 381(141) | 6(16) | 169(52) | 153(35) | [13.3,–0.4,6.0] | [13.4,–0.4,6.0] |
| 30 Nov A | 00 : 05 | 00 : 42 | 9(7) | 31 | 520 | 280(260) | 110(110) | 183(179) | 180(180) | [3.2,–7.7,–5.0] | [4.0,–8.4,–5.2] |
| 30 Nov B | 00 : 03 | 00 : 04 | 2(2) | 31 | 520 | 180(180) | 90(90) | 135(135) | 135(135) | [3.8,–8.8,–4.7] | [3.8,–8.8,–4.7] |

[a] $|E_{max}|$ and $|E_{min}|$ represent the maximum and minimum wave amplitudes (mV/m peak-peak) out of the set of burst captures in each row. The mean $|E_{mean}|$ and median $|E_{median}|$ values are calculated from all of the burst captures in each row. The values in the parentheses are for the subset of waves with clear comma-shaped polarization only. Also listed are the burst sample rate (kSamples/s), length of each individual burst (ms), and GSE start and end positions (in units of Earth radii) of the spacecraft during the time of the observations.

shock crossings concurrent with burst waveform captures occur during times of slow to moderate solar wind speed. Shock normal angles vary from quasi-parallel (STEREO-B on 6 November 2006, 14:48) to nearly perpendicular (STEREO-A on 6 November 2006 at 00:51). Of note is that large amplitude electric field burst waveforms, often up to a few hundred mV/m, are seen at all 13 listed shock crossings, regardless of shock normal angle. A majority of these bursts occur at the shock ramp (when a clear ramp is identifiable). Though the waves are bursty, their amplitudes usually far exceed the typical few tens of mV/m quasi-static electric field component [*Eastwood et al.*, 2007; *Dimmock et al.*, 2012].

[10] Four types of waveforms are seen during the bow shock crossings: electrostatic solitary waves, whistler mode waves, ion acoustic waves, and cyclotron harmonic waves. A small number of the burst captures show clear evidence of electrostatic solitary waves as reported by *Bale et al.* [1998]. These structures are usually immersed in a wavefield of a few mV/m. Well-isolated solitary waves are not commonly observed in the STEREO burst data set. Nearly all of the burst captures show at least some power at frequencies $f < f_{ce}$, where $f_{ce}$ is the electron cyclotron frequency, which, when elliptically polarized, suggests whistler mode waves. Occasionally, the whistler mode signal dominates the burst capture. However, a majority of the burst captures consist of large amplitude nonlinear fluctuations lasting for tens of milliseconds (few tens of wave cycles) with power peaked at $f > f_{ce}$. It is likely that some of this power is attributable to short wavelength ion acoustic waves Doppler-shifted in the spacecraft frame to higher frequencies. These show no tendency to be polarized along the magnetic field, consistent with observations by *Fuselier and Gurnett* [1984], *Balikhin et al.* [2005], and *Hull et al.* [2006].

[11] A majority of burst captures with peak power at $f > f_{ce}$ cannot be attributed solely to ion acoustic waves. These waveforms have broadband power spectra above $f_{ce}$ with significant power both parallel and perpendicular to the magnetic field resulting in distinctive "comma-shaped" polarizations. These waveforms are the focus of our study and their statistics are compiled separately in Table 1. A subset of these burst captures shows unambiguous evidence of multiple cyclotron harmonics and are identified as electron cyclotron harmonic waves. These are the first reported observations of electron cyclotron harmonic waves at the bow shock.

[12] Not listed in Table 1 are the four bow shock crossings on 12 December 2006 (two on each spacecraft) where no burst waveform captures were telemetered. STEREO TDSMax, a once-per-minute record of the maximum high-frequency electric field, indicates that large amplitude waves were indeed present on all four crossings. The lack of burst captures then suggests that they were overwritten by later large amplitude waveforms, like the extremely large amplitude whistler mode waves reported by *Cattell et al.* [2008], before they had a chance to be telemetered to the ground.

[13] Large amplitude waveforms with comma-shaped polarizations, enhanced broadband power at $f_{ce}$, and cyclotron harmonics were also observed on STEREO in the magnetosheath. Table 2 presents statistics of these burst captures.

[14] In the next sections we present a detailed analysis of burst captures with distinct electron cyclotron harmonics at two different bow shock crossings and a burst capture associated with a magnetic ramp-like structure in the magnetosheath, likely convected downstream from the bow shock.

### 3.1. STEREO Bow Shock Example

[15] We now discuss electron cyclotron harmonic waves observed at a bow shock crossing on STEREO-B and shown in Figure 1. Figure 1a plots IMPACT magnetometer data showing a bow shock crossing at 20:14 and a bow shock crossing or upstream structure from 20:28 to 20:40. Also plotted are the locations and amplitudes of the burst captures. All of the burst captures are clearly associated with magnetic field gradients. Each shows significant wave power at $f > f_{ce}$, with amplitudes up to 300 mV/m peak-peak. A few of the waves at and near the large magnetic field gradient at 20:14 show unambiguous cyclotron harmonics. Figure 1b shows a typical example of a waveform with cyclotron harmonics in a magnetic field-aligned coordinate system where the magnetic field points along $\hat{z}$ and the maximum variance direction lies in the $\hat{x}$-$\hat{z}$ plane. The waveforms are irregular and asymmetrical giving them a "choppy" quality. The spectra in Figure 1c show that the harmonics exist primarily perpendicular to the magnetic field. The parallel direction also contains significant wave power but without clear harmonics. Wave hodograms are presented in Figure 1d and have the distinctive comma shape in the maximum variance plane $\hat{x}$-$\hat{z}$. As indicated in Table 1, 21 of 38 burst captures at this bow shock crossing have comma-shaped polarizations. The polarizations for the remaining waveforms are linear (without an overall preference for orientation to the magnetic field, shock normal, or solar wind velocity) and complex (no preferred direction).

[16] For the example shown in Figure 1d, the comma-shaped polarization combined with the observation that the harmonics are perpendicular to the magnetic field suggest an

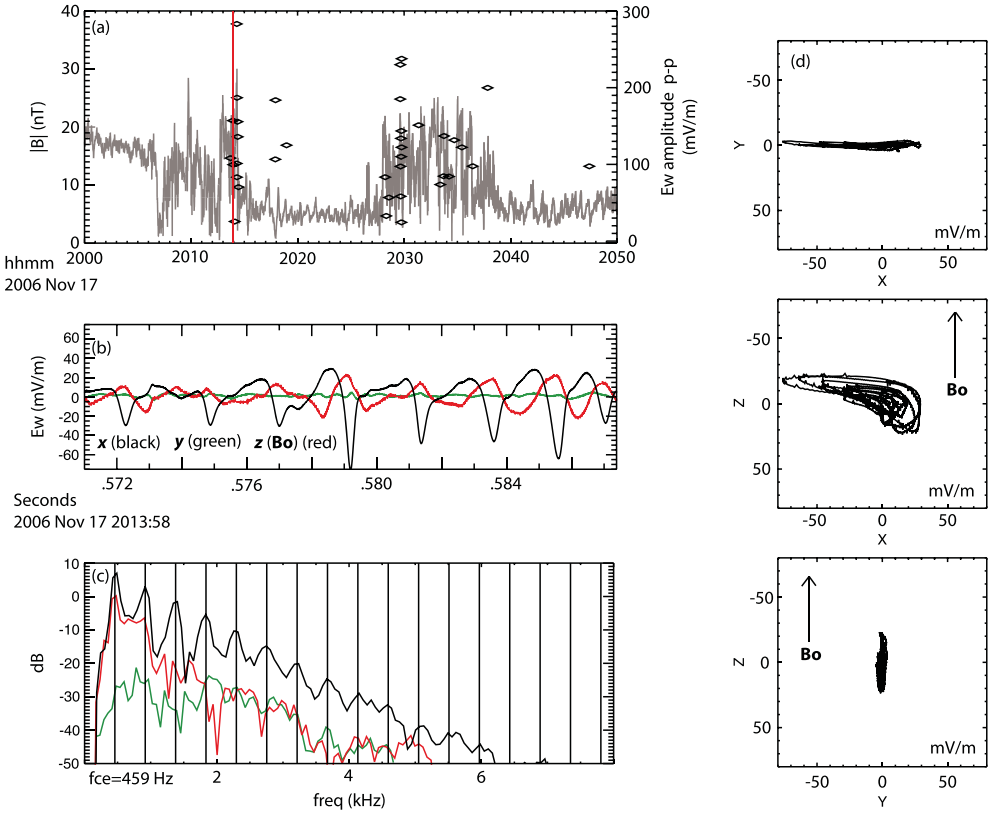


**Figure 1.** (a) STEREO-B observations at a bow shock crossing. The diamonds show the locations and amplitudes of the burst captures, many of which show clear signs of cyclotron harmonics. (b) Example burst waveform capture indicated by the red vertical line in Figure 1a. The waveform is in field-aligned coordinates where $\hat{z}$ is the magnetic field direction and the maximum variance electric field is in the $\hat{x}$-$\hat{z}$ plane. (c) Spectra of the burst waveform components showing clear cyclotron harmonics (black vertical lines) in the directions perpendicular to the magnetic field (black and green) but an absence of harmonics along the magnetic field. (d) Waveform hodograms indicating significant wave power in directions both parallel and perpendicular to the magnetic field.

interaction between two types of waves, a Bernstein wave perpendicular to the magnetic field and a field-aligned wave, possibly ion acoustic. Another possible explanation for the comma-shaped polarizations is waveform distortion due to electron trapping in large amplitude electric field waves as described by *Kellogg et al.* [2010, 2011].

### 3.2. Wind Bow Shock Example

[17] Our next example comes from Wind burst data during an inbound quasi-perpendicular bow shock crossing on 14 November 2001. Similar to Figure 1a, Figure 2a shows fluxgate magnetometer data of the shock crossing as well as the locations and amplitudes of the 11 burst captures, 7 at the magnetic ramp, with amplitudes (spin plane components only) from 80 to 510 mV/m peak-peak. Out of the these 11 burst captures, one contains discrete solitary waves and the rest have clear enhancements of power at or above $f_{ce}$ with evidence of cyclotron harmonics.

[18] Figure 2b shows an 80 mV/m peak-peak nonlinear waveform in the Wind spin plane at the ramp. The wavelet transform shows that the power is strongly peaked at $f_{ce}$ (as determined from Wind high-resolution magnetometer data). The spectra in Figure 2c show a clear pattern of harmonics on both antennas at nearly exact multiples of the local value of $f_{ce}$, particularly on the $E_y$ antenna. The magnetic field at this time is $\vec{B}_{\mathrm{GSE}} = [10, -10, 9]$ nT and is inclined from the spin axis $E_x$ antenna by ~42° and the $E_y$ antenna by ~90°. Thus, the harmonics are most distinct perpendicular to the magnetic field, similar to the STEREO example in Figure 1. As seen from Figure 2a, the wave is observed in a turbulent region where the magnetic field strength rapidly changes over a short distance. Thus, the close association of the first harmonic and $f_{ce}$ at the time of observation suggests that the wave is being observed close to its source. In addition, because the visible harmonics strongly peak at multiples of $f_{ce}$, there is likely little Doppler-shift, as would be observed if the wave propagated perpendicular to the solar wind flow. Three-dimensional waveform data are not available to explicitly show this but Figure 2d shows that the spin plane polarization is indeed primarily perpendicular to the solar wind velocity.

[19] The spectra in Figure 2c indicate that the response on the two Wind spin plane antennas is nearly identical at $f_{ce}$ but that the short ($E_y$) antenna has a stronger response at higher harmonics. This suggests two things: that the wavelength of the component $f = f_{ce}$ is longer than the long ($E_x$) antenna length of 100 m or else the response for this frequency would be stronger on the short $E_y$ antenna, and

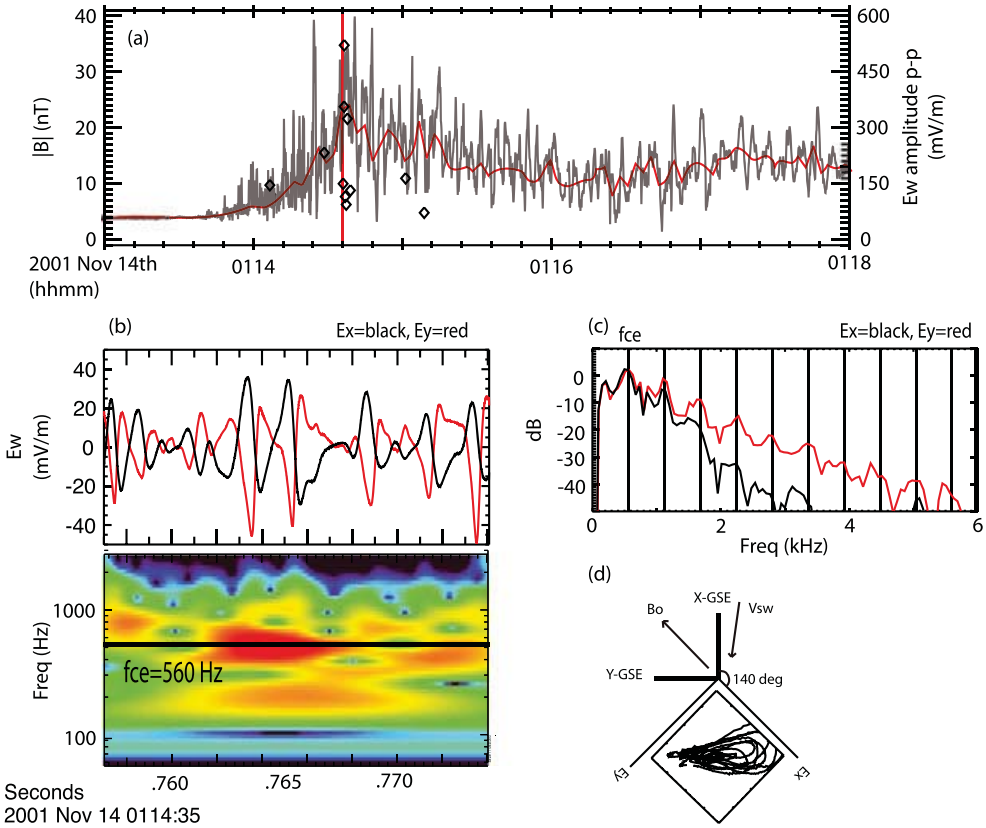


**Figure 2.** An example of a cyclotron harmonic wave in the context of a Wind bow shock crossing on 14 November 2001. (a) Wind magnetic fields investigation (MFI) high-resolution definitive data with overlain lower cadence magnetic field data in red to more clearly show the ramp region. The locations of all the burst captures are shown with the diamonds with peak-peak amplitudes given by the scale to the right. (b) The spin-plane electric field waveform components of the cyclotron harmonic wave at the magnetic ramp, indicated in Figure 2a by the vertical red line, along with the wavelet transform of the $E_y$ component. (c) Fast Fourier transform (FFT) of the waveform showing a peak in power at the local value of $f_{ce}$ as well as the first 10 harmonics (vertical black lines). (d) The spin-plane polarization of the waveform in Figure 2b. Wind antenna coordinates are shown by the axes labeled $E_x$ and $E_y$. Also shown are the solar wind velocity and magnetic field vectors. The spin-plane component is predominantly perpendicular to the solar wind velocity.

that the higher harmonics have wavelengths that are on the order of or shorter than 100 m. This estimated wavelength is roughly consistent with the electron cyclotron radius of ~500 m.

### 3.3. STEREO Magnetosheath Example

[20] We conclude this section with an analysis of a cyclotron harmonic wave observed by STEREO-B downstream of the bow shock in the magnetosheath at a magnetic field structure. Figure 3a shows that this structure lies between the bow shock and magnetopause. As with other large-scale magnetic structures in this region, it likely has its origin at the bow shock or upstream of it. Figure 3b is a close-up of this structure and shows the locations and amplitudes of the burst captures which are up to 100 mV/m peak-peak. Like those observed at the bow shock crossings, these waves are strongly associated with magnetic field enhancements and gradients. A majority of these burst waveforms have the distinctive comma-shaped polarization and show clear cyclotron harmonics, often most prominently in the directions perpendicular to the magnetic field. Past studies have shown electron cyclotron harmonic waves to be common both inside of the magnetosphere and near the magnetopause but fewer observations have been made within the magnetosheath near the bow shock [e.g., *Anderson et al.*, 1982] and these waves were not reported to be nearly as large in amplitude or to have any correlation with magnetic field gradients.

[21] Figures 3c–3e show an example of one of these waveforms in the same field-aligned coordinate system described previously. The irregular, asymmetric waveforms (Figure 3c) are similar to those seen at the bow shock which show signs of electron cyclotron harmonics. The FFTs in Figure 3d as well as the hodograms in Figure 3e are also very similar to those from waves at the bow shock. Namely, the power peaks just above $f_{ce}$, evidence of harmonics is most distinct in directions perpendicular to the magnetic field, and the hodograms show the typical comma-shaped polarization. Again, these results indicate that these waveforms are likely a combination of a perpendicular Bernstein wave and a parallel wave without harmonics. In this particular example there is significantly less power in the field-aligned

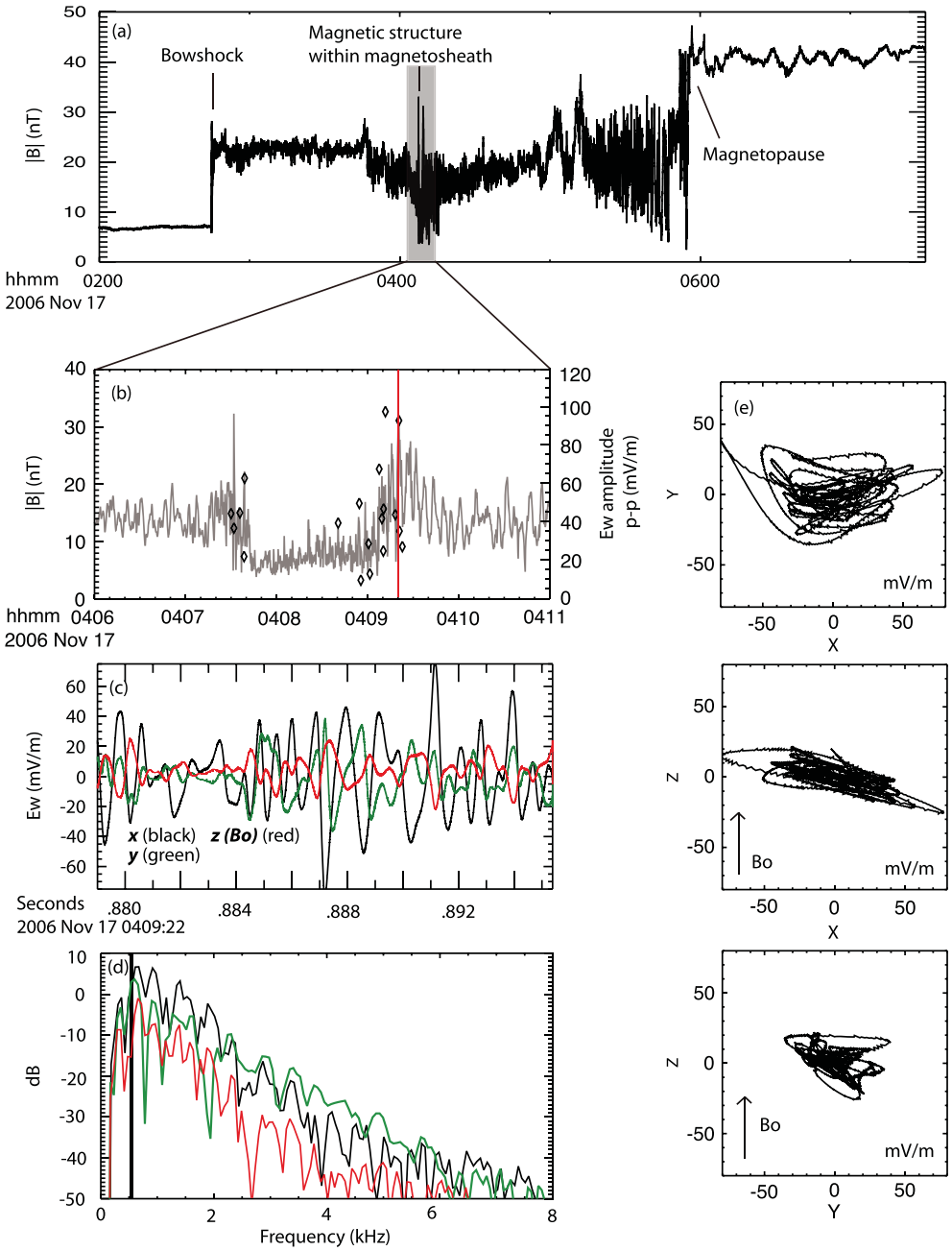


**Figure 3.** Example of a cyclotron harmonic wave observed on STEREO-B at a magnetic field structure inside of the magnetosheath. (a) The location of the structure relative to the bow shock and magnetopause is shown. (b) A closer look at the magnetic structure in the magnetosheath. The diamonds show the locations and amplitudes of the burst captures. (c) The burst waveform corresponding to the vertical red line in Figure 3b in field-aligned coordinates where $\hat{z}$ is the magnetic field direction and the maximum variance electric field is in the $\hat{x}$-$\hat{z}$ plane. (d) FFTs of the waveform. The local electron cyclotron frequency is indicated with the vertical black line. Evidence of harmonics can be seen in all three components but are most evident in the perpendicular directions. (e) Hodograms showing the comma-shape that is often associated with these waveforms.

direction, though this may be due to a local field rotation in this region of strong field gradient.

[22] Because of the similarities of these waves with those at the bow shock and the likelihood that this magnetic structure originated at the bow shock, we suggest that both sets of waves originate from the same free energy source. This is discussed in the following section.

## 4. Discussion

[23] We have presented a survey of STEREO and Wind burst captures in association with magnetic field gradients at the bow shock and downstream in the magnetosheath. Burst captures at the bow shock consist of three types of previously identified waves, ion acoustic waves, electrostatic solitary waves, and whistler mode waves, as well as newly

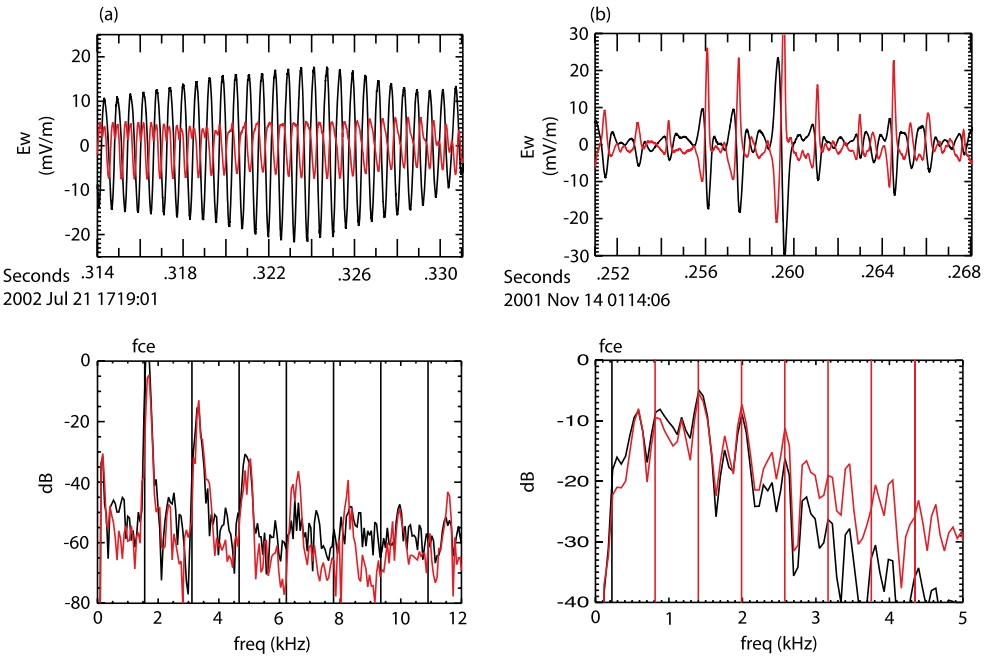


**Figure 4.** Comparison of Wind burst captures of waves with cyclotron harmonics (a) in the nightside magnetosphere at GSE=[–3,–6,–0.5] ($R_E$) and (b) at a bow shock crossing.

identified electron cyclotron harmonic waves. Cyclotron harmonic waves were also observed just downstream of the bow shock at magnetic field gradients in the magnetosheath. These waves are easily identified by their distinctive comma-shaped polarizations in the plane containing the magnetic field and maximum variance electric field. The variety of bow shock crossing locations (and hence shock normal angles) with these cyclotron harmonic waveforms (Table 1) suggests that they may be ubiquitous at the bow shock and also within the magnetosheath (Table 2).

### 4.1. Comparison With Traditional Bernstein Waves

[24] The waveforms we have presented show signs of cyclotron harmonics yet they differ from typical Bernstein waves of the sort observed within the magnetosphere in a couple of important ways. Figure 4 shows a Wind burst comparison between a more typical Bernstein wave, observed in the nightside magnetosphere and a cyclotron harmonic wave observed at the bow shock. Some differences are immediately apparent. FFTs show that both waves have harmonically spaced peaks in power. The traditional Bernstein wave in Figure 4a has power strongly focused at these peaks with little power at other frequencies. In this particular example a majority of the total wave power is near $f_{ce}$, giving the waveform a sinusoidal quality. The bow shock FFTs, in contrast, have significant wave power off-peak as is seen in Figure 4b. These waveforms typically have a choppy, asymmetrical quality.

[25] Another difference is seen by comparing polarizations. Traditional Bernstein waves tend to show simple polarization, primarily perpendicular to the magnetic field. The bow shock cyclotron harmonic waveforms, in contrast, often have a complex comma-shaped polarization with significant power both parallel and perpendicular to the magnetic field (e.g., Figures 1d and 3e). Since harmonics tend to be more prominent in the directions perpendicular to the magnetic field, this suggests an interaction between two waves, a perpendicular Bernstein wave, and a parallel wave without harmonics. One likely candidate for the parallel wave is ion acoustic waves which have been shown to be ubiquitous at the bow shock.

[26] These observations suggest a fundamental difference between traditional Bernstein waves and the waves observed at the bow shock. The differences may be due to the generation mechanism. Traditional Bernstein waves are known to grow from loss cone distributions [*Horne and Thorne*, 2000] while the bow shock waves, given their close association with magnetic field gradients, likely get their free energy from beam sources.

[27] A possible generation mechanism is the electron cyclotron drift instability (ECDI) [*Forslund et al.*, 1970] which involves the coupling of Bernstein and ion beam modes that occurs when, for example, shock-incident electrons see (in their rest frame) ion acoustic waves from shock-reflected ions Doppler-shifted to near $f_{ce}$. This can result in a strong interaction between electron and ion species. A recent particle-in-cell simulation by *Muschietti and Lembège* [2013], designed for conditions that allow the growth of small-scale waves (realistic values of the proton to electron mass ratio, the plasma to electron cyclotron frequency ratio, etc.), has indicated that the ECDI may be much more important than previously thought at the bow shock transition region. The waveforms in this paper are consistent with those in *Muschietti and Lembège* [2013]. Namely, the estimated wavelength of a few times 100 m is consistent with that predicted ($\lambda \sim 60\lambda_D$), power is observed to peak in close association with $f_{ce}$, and the comma-shaped polarizations indicate the presence of both Bernstein waves and ion acoustic waves. Thus, the ECDI represents a possible source for these waves.

[28] The simulations by *Muschietti and Lembège* [2013] indicated that the ECDI has an inverse cascade of harmonics with time, i.e., the frequency range of unstable harmonics decreases with time. Our observations indicate that the lower harmonics tend to dominate over higher harmonics, suggesting that large amplitude ECDI waves are formed during later stages of ECDI evolution.

[29] This study represents the first observational evidence that the ECDI may occur at the bow shock. The only prior observation was presented by *Wilson et al.* [2010], who reported ECDI waves from Wind burst data at an interplanetary shock. Future validation of the ECDI at the bow shock and magnetosheath is important because, as pointed out by *Muschietti and Lembège* [2013], ECDI waves, though they carry only a small fraction of the energy density of the electron and ion beams, are expected to be effective at transferring energy and momentum between the species, ultimately resulting in energy dissipation. True validation of the ECDI may be addressed from a more detailed analysis of the Wind burst data set in conjunction with particle data.

### 4.2. Identification of Cyclotron Harmonic Waves

[30] We conclude with a discussion of the identification of electron cyclotron waves at the bow shock. Our study is similar in many ways to *Hull et al.* [2006] who analyzed high time resolution waveform data from Polar at the bow shock during a time of extremely high solar wind velocity. Their analysis identified waves from 100 to 4000 Hz with amplitudes of up to 80 mV/m, lasted from 10 to 30 cycles, and were observed at magnetic field gradients. An interferometric analysis showed phase velocities consistent with the ion acoustic speed and wavelengths of roughly half the electron cyclotron radius. The authors thus concluded that the waveforms were likely ion acoustic. This result is consistent with past studies that identified ion acoustic waves as the primary component of wave power at >200 Hz near the bow shock ramp [*Rodriguez and Gurnett*, 1975; *Wygant et al.*, 1987] and at interplanetary shocks [*Wilson et al.*, 2007].

[31] We note, however, that waveform properties determined by *Hull et al.* [2006] are also consistent with those of cyclotron harmonic waves observed in this study. When harmonics are not apparent and polarization is not predominantly along the magnetic field, it can be difficult to distinguish between cyclotron harmonic waves and Doppler-shifted ion acoustic waves, though power spectra above $f_{ce}$ tend to be broader for the cyclotron harmonic waves than for traditional ion acoustic waves [e.g., *Wilson et al.*, 2010, Figure 10] and they typically exhibit the comma-shaped polarization discussed previously. More sophisticated analysis techniques [e.g., *Giagkiozis et al.*, 2011] may be needed to identify the difference between these two types of waves when clear harmonics are not present.

[32] We now discuss reasons why the unambiguous identification of harmonics may be difficult even when the burst captures in fact contain cyclotron harmonic waves. The first difficulty is that, as discussed previously, the instability that generates these waves may involve a combination of cyclotron harmonic waves and ion acoustic waves, for example, in the ECDI. Ion acoustic waves are often not polarized strictly along the magnetic field [e.g., *Fuselier and Gurnett*, 1984; *Hull et al.*, 2006] and may make a significant contribution to the perpendicular wave power, tending to mask harmonics which may otherwise be distinct.

[33] A second difficulty involves details of which harmonics are unstable. In both the traditional Bernstein instability and the ECDI unstable frequencies can, depending on conditions, fall anywhere from $nf_{ce}$ to $(n + 1)f_{ce}$ where $n$ is an integer, and successive harmonics are not necessarily multiples of the first harmonic. As an example, *Muschietti and Lembège* [2013, Figure 2] show that the frequency of each unstable harmonic for the ECDI depends on the speed of the shock-reflected ions, and the unstable frequencies will not be exact harmonics of $f_{ce}$. This often does not present an obstacle toward identifying traditional Bernstein waves (as in Figure 4a) because the harmonics can dominate the spectrum but can be for the cyclotron harmonic waves observed at the bow shock (as in Figure 4b) because the harmonics do not dominate the spectrum to the same extent.

[34] Finally, even if the unstable frequencies are exact multiples of the fundamental and are confined to the perpendicular plane, we still may not be able to observe them for the following reason. Cyclotron harmonic waves tend to be short wavelength and thus can be significantly Doppler-shifted by the solar wind flow past the observing spacecraft. When these waveforms propagate with a component along the solar wind velocity, higher harmonics, which have shorter wavelengths, can be Doppler-shifted more than lower harmonics. This effect will tend to mask the presence of harmonics. If there is to be any hope of observing a preserved harmonic spacing in power, the wave vector must be largely perpendicular to the solar wind velocity. This is the case with the examples presented in this paper but is not expected to be the case in general. The above reasons show that we are able to detect the presence of cyclotron harmonics in waves with comma-shaped polarizations only under special circumstances.

[35] Waves with comma-shaped polarizations are the most common type of wave seen during the STEREO bow shock crossings, regardless of bow shock geometry, which suggests that they are a common feature of the bow shock transition region. Furthermore, ion acoustic waves at the bow shock may often be coupled to Bernstein waves via the ECDI.

## 5. Conclusions

[36] We have presented the first observations of electron cyclotron harmonic waves at the Earth's bow shock. The waves are large amplitude (up to >500 mV/m peak-peak) and are observed at magnetic field gradients at nearly every bow shock crossing, regardless of the shock normal angle. These waves are also observed in the magnetosheath in association with a magnetic field structure, likely convected downstream from the bow shock.

[37] The cyclotron harmonics are often most prominent in the directions perpendicular to the magnetic field. FFTs of Wind burst captures with electron cyclotron harmonics often show a similar response on both the short (15 m) and long (100 m) spin plane antenna at low harmonics, but with a decreasing response on the long antenna at higher harmonics. This indicates that the first harmonic has a wavelength of a few times 100 m, consistent with the electron cyclotron radius.

[38] The burst captures generally have significant power along the magnetic field direction as well as perpendicular to it, resulting in a distinctive comma-shaped polarization. These observations suggest that the waves are a combination of a perpendicular Bernstein wave and a parallel ion acoustic wave. The most likely mechanism for the creation of these waves is the electron cyclotron drift instability which has recently been predicted to occur at the bow shock.

[39] Our observations show that a majority of burst waveform captures observed by STEREO during the bow shock crossings exhibit this comma-shaped polarization, outnumbering other types of high-frequency waves previously identified like whistler mode waves, ion acoustic waves, and electrostatic solitary waves. Therefore, we expect that they are an important component of the high-frequency electrostatic spectrum at the bow shock.

## Appendix A: TDS Signal Calibration

[40] In this appendix we discuss the calibration of the TDS electric field data, first on STEREO and then on Wind.

[41] The measurement of external electric field signals by the TDS on each STEREO spacecraft involves the coupling of the antenna to the signal and the spacecraft body, and the modification of the signal as it proceeds through the physical circuitry of the preamplifier and the TDS instrument with its 16 bit analog-to-digital converter. Ignoring for the moment details of the antenna coupling, a signal measured by an antenna arrives at the front end of the preamplifier as the time-dependent voltage $V_{\text{in}}(t)$. It then passes through the preamplifier and is then converted to counts as a function of time $N(t)$ by the analog-digital converter in the TDS. This signal is related to the input voltage via the equation $V_{\text{in}}(t) = N(t)\left(\frac{\pm 2.5 \text{ volts}}{2^{16}}\right)$, where the last term is the resolution of the 16-bit analog-to-digital converter. The frequency-dependent gains of the preamplifier and the TDS circuitry are then applied to the Fourier transform of the signal via $\text{FFT}(V_{\text{in}}(t))\left(\frac{1}{G_{\text{preamp}} G_{\text{TDS}}}\right)$ and the result is inverse transformed back to the time domain giving $V_{\text{out}}$. This procedure is applied to the signal on each antenna. This calibration is straightforward and depends only on the characteristics of the physical circuitry.

[42] The conversion of $V_{\text{out}}$ to an electric field on each antenna is given by the equation $E_{\text{out}} = V_{\text{out}}/L_{\text{eff}}$, where $L_{\text{eff}}$ is the effective antenna length, also known as the "electrical length." The effective length differs from the physical antenna length due to shorting effects from the finite antenna capacitance $C_A$, antenna coupling to the plasma sheath resistance $R_S$ and capacitance $C_S$, antenna coupling to the antenna enclosures via the base resistance $R_B$ and capacitance $C_B$, and the capacitance of the antenna cable and preamp input (bundled up with $C_B$ in the term $C_{\text{stray}}$) [*Bale et al.*, 2008, Figure 2]. A proper measurement of a three-dimensional electric field signal requires knowledge of the frequency-dependent effective lengths of each antenna to determine wave amplitude, and the frequency-dependent effective angles between the antennas which allows the rotation of the data from the antenna coordinate system into the orthogonal spacecraft coordinate system via the equation below Figure 14 of *Bale et al.* [2008].

[43] At high frequencies $f >> f_{pe}$, where $f_{pe}$ is the electron plasma frequency, the antennas are in the capacitively coupled regime where they are weakly coupled to the plasma and the antenna gain is described by $G \sim C_A/(C_A + C_{\text{stray}}) \sim 1/2$. The effective lengths and angles at these frequencies are constant over a large frequency range and are well determined [*Bale et al.*, 2008, Figure 14].

[44] At lower frequencies an external field is coupled to the antennas through the plasma sheath resistance $R_S$ and capacitance $C_S$. At very low frequencies (less than a few hundred Hz) the system enters the resistively coupled regime where $C_S$ can be ignored but $R_S$ is important. The gain in this regime is given by $G \sim R_B/(R_B + R_S)$. $R_S$ is a sensitive function of the electron thermal current but its effect can be minimized by maximizing the base resistance. This was not done on STEREO, however, because the accurate measurement of low-frequency electric fields was not a high mission priority. The fundamental frequency of the harmonic waves presented in this paper ranges from a few hundred Hz to a few kHz, near the estimated transition from the capacitively to resistively coupled regimes. We have determined that the variation in the effective antenna lengths and angles from their capacitively coupled values at these frequencies is minimal for the observed waves, and thus, we have used the effective antenna lengths and angles defined in *Bale et al.* [2008, Figure 14].

[45] Contrary to STEREO, the Wind antennas measure the cyclotron harmonic waveforms in the capacitative coupling regime where the effective lengths are well determined. From the start of the mission until 3 August 2000, the effective lengths were 43 m for the long (100 m physical length) tip-tip spin plane antenna and 4.5 m for the short (15 m physical length) tip-tip spin plane antenna. However, the long antenna was partially sheared off by a dust impact on 3 August 2000, reducing its effective length to 28 m. This occurred again on 25 September 2002, further reducing its effective length to 25 m. The effective length of the short spin plane antenna is unchanged from its original value. The Wind TDS observations presented in this paper are from 14 November 2001, and thus, we used effective lengths of 28 m and 4.5 m.

## Appendix B: Instrumental Response to Short Wavelengths

[46] Since it is possible for harmonics to be an artificial instrument response we now show that the harmonics are indeed a real phenomenon.

[47] There are two processes in which an antenna/receiver can artificially produce harmonics in response to an input signal. The first involves electronic nonlinearities created when an antenna responds to a large amplitude input signal. The antennas on STEREO and Wind were designed to respond linearly to large amplitude waves of the type presented in this paper. It is unlikely that either antenna system would create harmonics at the mV/m level in response to large amplitude (but unclipped) waveforms.

[48] The second process involves a harmonically varying antenna response to waves with wavelengths on the order of or shorter than the effective antenna length $L_{\text{eff}}$, as discussed in Appendix A. The antenna response at the preamp input is $\delta V_{\text{in}}/E_o L_{\text{eff}}$, where $E_o$ is the applied electric field. The

response is a function of the normalized wave number $x = kL_{\text{eff}}/2$ and is plotted in *Gurnett* [1998, Figure 9] for a cylindrical dipole. Note that the Wind antennas are cylindrical dipoles but the STEREO antennas are cylindrical monopoles with the spacecraft body acting as a grounded plane. *Bale et al.* [2008] showed that this is a good approximation to a dipole if the antenna is grounded to the spacecraft body by a base capacitance $C_B$ of 32 pF. This effect is accounted for implicitly via the usage of the effective lengths determined by *Bale et al.* [2008] in calibrating the burst waveforms. Values of the normalized wave number less than unity result in a continuously decreasing antenna response as a function of frequency while values greater than unity result in a harmonically varying antenna response.

[49] We now calculate the normalized wave number $x$ by assuming that the wavelengths of the cyclotron harmonic waves are roughly the electron cyclotron radius ($\sim$ 500 m), consistent with the observed antenna response on Wind. This gives us a wave number of $k \sim 12$ km$^{-1}$. For the short STEREO antennas ($L_{\text{eff}} \sim$1.2 m) the normalized wave number is $x < 0.01 << 1$ and the antenna response to this wave will be a smoothly decreasing function of frequency. For the longer Wind spin plane antenna ($L_{\text{eff}} = 28$ m) and shorter spin plane antenna ($L_{\text{eff}} = 4.5$ m), the normalized wave numbers are $x \sim 0.2$ and $x \sim 0.03$, respectively. Thus, the Wind antennas, like the STEREO antennas, will respond as a smoothly decreasing function of frequency. Higher harmonics have larger wave numbers and if we extend this analysis out to the third harmonic, then we have a wave number of $k = 2^3 \cdot 12$ km$^{-1}$ and an effective wave number of $x \sim 0.2$ for the short antenna pair which will still result in a smoothly varying frequency response. For wavelengths much shorter than 500 m, the response on long Wind spin plane antenna may exceed unity. However, the effective lengths of the two Wind spin plane antennas differ by a factor of nearly 7. This means that the harmonic response of each antenna will be different and it is unlikely that both antennas would see the same harmonics, as is typically observed, if they were artificial.

[50] Finally, we have shown that the harmonics are more likely to be observed in the directions perpendicular to the magnetic field than parallel to it. Artificial harmonics are unlikely to be organized in this manner. The above considerations indicate that the harmonics are innate to the burst waveforms and not artificially created.

[51] **Acknowledgments.** Simulation results have been provided by the Community Coordinated Modeling Center at Goddard Space Flight Center through their public Runs on Request system (http://ccmc.gsfc.nasa.gov). The CCMC is a multiagency partnership between NASA, AFMC, AFOSR, AFRL, AFWA, NOAA, NSF, and ONR. The BATS-R-US Model was developed by the Space Weather Research Center at the NASA Goddard Space Flight Center. This research was supported by NASA grants NNX12AB23G and NNX10AU82G.

[52] Philippa Browning thanks Forrest Mozer and an anonymous reviewer for their assistance in evaluating this paper.

## References

Anderson, R. R., T. E. Eastman, C. C. Harvey, M. M. Hoppe, B. T. Tsurutani, and J. Etcheto (1982), Plasma waves near the magnetopause, *J. Geophys. Res.*, *87*, 2087–2107, doi:10.1029/JA087iA04p02087.

Bale, S. D., P. J. Kellogg, D. E. Larson, R. P. Lin, K. Goetz, and R. P. Lepping (1998), Bipolar electrostatic structures in the shock transition region: Evidence of electron phase space holes, *Geophys. Res. Lett.*, *25*, 2929–2932, doi:10.1029/98GL02111.

Bale, S. D., et al. (2008), The electric antennas for the STEREO/WAVES experiment, *Space Sci. Rev.*, *136*, 529–547.

Balikhin, M., S. Walker, R. Treumann, H. Alleyne, V. Krasnoselskikh, M. Gedalin, M. Andre, M. Dunlop, and A. Fazakerley (2005), Ion sound wave packets at the quasiperpendicular shock front, *Geophys. Res. Lett.*, *32*, L24106, doi:10.1029/2005GL024660.

Bougeret, J.-L., et al. (1995), Waves: The radio and plasma wave investigation on the Wind spacecraft, *Space Sci. Rev.*, *71*, 231–263, doi:10.1007/BF00751331.

Bougeret, J. L., et al. (2008), S/WAVES: The radio and plasma wave investigation on the STEREO mission, *Space Sci. Rev.*, *136*, 487–528, doi:10.1007/s11214-007-9298-8.

Cattell, C., et al. (2008), Discovery of very large amplitude whistler-mode waves in Earth's radiation belts, *Geophys. Res. Lett.*, *35*, L01105, doi:10.1029/2007GL032009.

Dimmock, A. P., M. A. Balikhin, V. V. Krasnoselskikh, S. N. Walker, S. D. Bale, and Y. Hobara (2012), A statistical study of the cross-shock electric potential at low Mach number, quasi-perpendicular bow shock crossings using Cluster data, *J. Geophys. Res.*, *117*, A02210, doi:10.1029/2011JA017089.

Eastwood, J. P., S. D. Bale, F. S. Mozer, and A. J. Hull (2007), Contributions to the cross shock electric field at a quasiperpendicular collisionless shock, *Geophys. Res. Lett.*, *34*, L17104, doi:10.1029/2007GL030610.

Fairfield, D. H. (1974), Whistler waves observed upstream from collisionless shocks, *J. Geophys. Res.*, *79*, 1368–1378, doi:10.1029/JA079i010p01368.

Formisano, V., and R. Torbert (1982), Ion acoustic wave forms generated by ion-ion streams at the Earth's bow shock, *Geophys. Res. Lett.*, *9*, 207–210, doi:10.1029/GL009i003p00207.

Forslund, D. W., R. L. Morse, and C. W. Nielson (1970), Electron cyclotron drift instability, *Phys. Rev. Lett.*, *25*, 1266–1270, doi:10.1103/PhysRevLett.25.1266.

Fredricks, R. W., G. M. Crook, C. F. Kennel, I. M. Green, F. L. Scarf, P. J. Coleman, and C. T. Russell (1970), OGO 5 observations of electrostatic turbulence in bow shock magnetic structures, *J. Geophys. Res.*, *75*, 3751–3768, doi:10.1029/JA075i019p03751.

Fuselier, S. A., and D. A. Gurnett (1984), Short wavelength ion waves upstream of the Earth's bow shock, *J. Geophys. Res.*, *89*, 91–103, doi:10.1029/JA089iA01p00091.

Giagkiozis, I., S. N. Walker, and M. A. Balikhin (2011), Dynamics of ion sound waves in the front of the terrestrial bow shock, *Ann. Geophys.*, *29*, 805–811, doi:10.5194/angeo-29-805-2011.

Gurnett, D. A. (1998), Principles of space plasma wave instrument design, in *Measurement Techniques for Space Plasmas: Fields,* Monograph 103, edited by R. Pfaff, J. Borovsky, and J. Young, pp. 121–136, AGU, Washington, D. C.

Horne, R. B., and R. M. Thorne (2000), Electron pitch angle diffusion by electrostatic electron cyclotron harmonic waves: The origin of pancake distributions, *J. Geophys. Res.*, *105*, 5391–5402, doi:10.1029/1999JA900447.

Hull, A. J., D. E. Larson, M. Wilber, J. D. Scudder, F. S. Mozer, C. T. Russell, and S. D. Bale (2006), Large-amplitude electrostatic waves associated with magnetic ramp substructure at Earth's bow shock, *J. Geophys. Res.*, *33*, L15104, doi:10.1029/2005GL025564.

Kellogg, P. J., C. A. Cattell, K. Goetz, S. J. Monson, and L. B. Wilson III (2010), Electron trapping and charge transport by large amplitude whistlers, *Geophys. Res. Lett.*, *372*, L20106, doi:10.1029/2010GL044845.

Kellogg, P. J., C. A. Cattell, K. Goetz, S. J. Monson, and L. B. Wilson III (2011), Large amplitude whistlers in the magnetosphere observed with Wind-Waves, *J. Geophys. Res.*, *116*, A09224, doi:10.1029/2010JA015919.

Lepping, R. P., et al. (1995), The wind magnetic field investigation, *Space Sci. Rev.*, *71*, 207–229, doi:10.1007/BF00751330.

Luhmann, J. G., et al. (2008), STEREO IMPACT investigation goals, measurements, and data products overview, *Space Sci. Rev.*, *136*, 117–184.

Muschietti, L., and B. Lembège (2013), Microturbulence in the electron cyclotron frequency range at perpendicular supercritical shocks, *J. Geophys. Res. Space Physics*, *118*, 2267–2285, doi:10.1002/jgra.50224.

Ogilvie, K. W., et al. (1995), SWE, A comprehensive plasma instrument for the Wind spacecraft, *Space Sci. Rev.*, *71*, 55–77, doi:10.1007/BF00751326.

Papadopoulos, K. (1985), Microinstabilities and anomalous transport, in *Collisionless Shocks in the Heliosphere: A Tutorial Review,* vol. 34, edited by R. G. Stone and B. T. Tsurutani, pp. 59–90, AGU, Washington, D. C.

Rodriguez, P., and D. A. Gurnett (1975), Electrostatic and electromagnetic turbulence associated with the Earth's bow shock, *J. Geophys. Res.*, *80*, 19–31, doi:10.1029/JA080i001p00019.

Sauvaud, J.-A., et al. (2008), The IMPACT Solar Wind Electron Analyzer (SWEA), *Space Sci. Rev.*, *136*, 227–239, doi:10.1007/s11214-007-9174-6.

Slavin, J. A., and R. E. Holzer (1981), Solar wind flow about the terrestrial planets. I - Modeling bow shock position and shape, *J. Geophys. Res.*, *86*, 11,401–11,418, doi:10.1029/JA086iA13p11401.

Wilson, L. B., III, C. Cattell, P. J. Kellogg, K. Goetz, K. Kersten, L. Hanson, R. MacGregor, and J. C. Kasper (2007), Waves in interplanetary shocks: A Wind/WAVES study, *Phys. Rev. Lett.*, *99*, 041101, doi:10.1103/PhysRevLett.99.041101.

Wilson, L. B., III, C. A. Cattell, P. J. Kellogg, K. Goetz, K. Kersten, J. C. Kasper, A. Szabo, and M. Wilber (2010), Large-amplitude electrostatic waves observed at a supercritical interplanetary shock, *J. Geophys. Res.*, *115*, A12104, doi:10.1029/2010JA015332.

Wygant, J. R., M. Bensadoun, and F. S. Mozer (1987), Electric field measurements at subcritical, oblique bow shock crossings, *J. Geophys. Res.*, *92*, 11,109–11,121, doi:10.1029/JA092iA10p11109.